PAPER • OPEN ACCESS

Ultra-fast 3D printing of assembly—free complex optics with sub-nanometer surface quality at mesoscale

To cite this article: Shuai Peng *et al* 2023 *Int. J. Extrem. Manuf.* **5** 035007

View the article online for updates and enhancements.

Ultra-fast 3D printing of assembly—free complex optics with sub-nanometer surface quality at mesoscale

Shuai Peng[1]**, Jiawen Xu**[1]**, Dongya Li**[1,2]**, Jun Ren**[1]**, Meng Zhang**[1]**, Xiaolong Wang**[3,*] **and Yu Liu**[1,2,*] (ORCID)

[1] School of Mechanical Engineering, Jiangnan University, 214122 Wuxi, People's Republic of China
[2] Jiangsu Key Lab of Advanced Food Manufacturing Equipment and Technology, Jiangnan University, 214122 Wuxi, People's Republic of China
[3] State Key Laboratory of Solid Lubrication, Lanzhou Institute of Chemical Physics, Chinese Academy of Sciences, 730000 Lanzhou, People's Republic of China

E-mail: wangxl@licp.cas.cn and yuliu@jiangnan.edu.cn

CrossMark

Abstract

Complex-shaped optical lenses are of great interest in the areas of laser processing, machine vision, and optical communications. Traditionally, the processing of complex optical lenses is usually achieved by precision machining combined with post-grinding or polishing, which is expensive, labor-intensive and difficult in the processing of ultra-complex optical lenses. Additive manufacturing is an emerging technology that provides significant advantages in producing highly intricate optical devices. However, the layer-by-layer method employed in such manufacturing processes has resulted in low printing speeds, as well as limitations in surface quality. To address these challenges, we apply tomographic volumetric printing (TVP) in this work, which can realize the integrated printing of complex structural models without layering. By coordinating the TVP and the meniscus equilibrium post-curing methods, ultra-fast fabrication of complex-shaped lenses with sub-nanometric roughness has been achieved. A 2.5 mm high, outer diameter 9 mm spherical lens with a roughness value of RMS = 0.3340 nm is printed at a speed of 3.1×10^4 mm^3 h^{-1}. As a further demonstration, a complex-shaped fly-eye lens is fabricated without any part assembly. The designed spherical lens is mounted on a smartphone's camera, and the precise alignments above the circuit board are captured. Upon further optimization, this new technology demonstrates the potential for rapid fabrication of ultra-smooth complex optical devices or systems.

Supplementary material for this article is available online

Keywords: tomographic volumetric printing, meniscus equilibrium post-curing methods, spherical lens sub-nanometric roughness

1. Introduction

Optical devices with excellent illumination, sensing, light modulating, and display capabilities [1] can be directly applied to sensors [2], hologram reconstruction [3], human-computer interaction [4], and other optoelectronics [5]. Traditional manufacturing methods for optical devices primarily comprise precision machining [6], casting, and injection molding [7]. However, the current mainstream processing technologies cannot satisfy the ultra-complex structure and ultra-smooth surface quality of advanced optical devices, which is inevitable to limit the further development of optical components in broader functional applications. Lately, three-dimensional (3D) printing [1, 8–19] has been attracting significant attention for creating highly complex shapes of optical devices.

The manufacturing efficiency of optical components, especially optical lenses, is usually determined by the printing speed and surface smoothness. Digital light processing (DLP) [9–13] which uses a single layer as the basic manufacturing unit is considered to be a more productive method for the fabrication of polymer lenses in comparison with dot printing-based two-photon polymerization [14, 15], fused deposition modeling [16], direct ink writing [17], and stereolithography (SLA) [18]. However, most of the processing time is consumed in reapplying new light-curing resin to ensure uniformity between layers. The continuous liquid interface production (CLIP) process [19], which eliminates the time-consuming recoating step, offers an opportunity to increase manufacturing speed significantly. However, although CLIP dramatically increased the printing speed, the surface quality of optical lenses obtained is still constrained by the step effect. Therefore, the methods of mechanical oscillation assistance [10], grayscale polymerization method [12], post-coating [20], and meniscus equilibrium post-curing method [11, 21–24] have been developed for reducing the roughness of the surface down to the nanometer level. Among them, meniscus equilibrium post-curing method which requires no extra-facility is a convenient and effective way to improve the surface quality.

A revolutionary additive manufacturing technology called volumetric 3D printing [25–35] has been invented recently, which prints all points of the target region simultaneously in a specific container of precursor material through three typical approaches: holographic exposure [25, 26], orthogonal superposition [27], and tomographic volumetric 3D printing [28–35]. More specially, tomographic volumetric 3D printing polymerizes 3D structures by projecting two-dimensional (2D) light patterns calculated by radon transformation. After continuous projection of the 2D light patterns into the rotating resin container, the photopolymerization reaction occurs in the liquid resin of the target space where the light dose exceeds the cross-linking threshold.

Tomographic volumetric printing (TVP) has several advantages for printing high-viscosity resin materials at ultra-high speed. During the printing process, little relative motion is observed between the liquid resin and the manufactured object, which facilitates the accuracy of light dose delivery to the target space. Therefore, high-viscosity precursor materials can be used. The process guarantees a high surface quality of the surface while printing complex geometric structures in a single light pass. Furthermore, no sacrificial solid support structure is required since the 3D object is formed inside the viscous precursor material during printing. Given the unique advantages, TVP is desirable for fabricating complex optical devices. However, very few research results have been reported concerning the study of TVP in the optical manufacturing field.

In this work, we explore the viability of utilizing the TVP process further to improve the 3D printing speed of complex optical lenses. For a direct building of a centimeter-scale optical lens with sub-nanometer surface quality, the TVP technology first generates the lens structure in a few seconds. After extracting the manufactured object from the container, the resin film remaining on its surface is further cured to feature an ultra-smooth surface at the sub-nanometer scale. Fabrication of several examples of optical lenses will be illustrated about the advance of our developed process.

2. Methods

2.1. TVP system

The delivery of light dose is accomplished by irradiating the 2D light patterns into the rotating resin vial, as shown in figure 1(a). In TVP, each voxel in the target space has only two states—whether it reaches the gel point. A popular way to calculate the sets of TVP projection images is by using gradient-descent optimization algorithm [28], which is a better method to optimize the reconstructed optical dose. In our study, the TVP system primarily consists of a computer for processing control, a projector, a precision rotating stage, a charge coupled device (CCD) camera, a red light emitting diode (LED) and a cylindrical resin container. The specific model of the TVP hardware is detailed in section 5. To reduce the refraction of the light beam, we immersed the container in a rectangular tank containing the index-matching fluid, as shown in figure S1 of supplementary materials. Figure 1(a) illustrates that the serialized 2D light patterns are projected into the cylindrical container containing the mixed acrylic resin and photoinitiator (see details in section 5). The inset shows a frame of the projection. To observe the process of solidification of the target object, a red-light source illuminates the inside of the container during printing. The red-light source is orthogonal to the light from the projector, with the intersection point located at the center of the cylindrical container. Intensity spectra of the blue channels of the projector and red led are obtained using a spectrometer, as shown in figure S2. A CCD camera is used to observe the contents of the container.

At the beginning of printing, the liquid resin does not experience a cross-linking reaction after the brief stimulation of the projection light. The reason for this nonlinear solidification behavior in the target space is the presence of oxygen inhibition in the free radical polymerization process. The consumption of oxygen molecules by the radicals in the intended resin region is essential before photopolymerization can commence. Therefore, before photopolymerization occurs, the
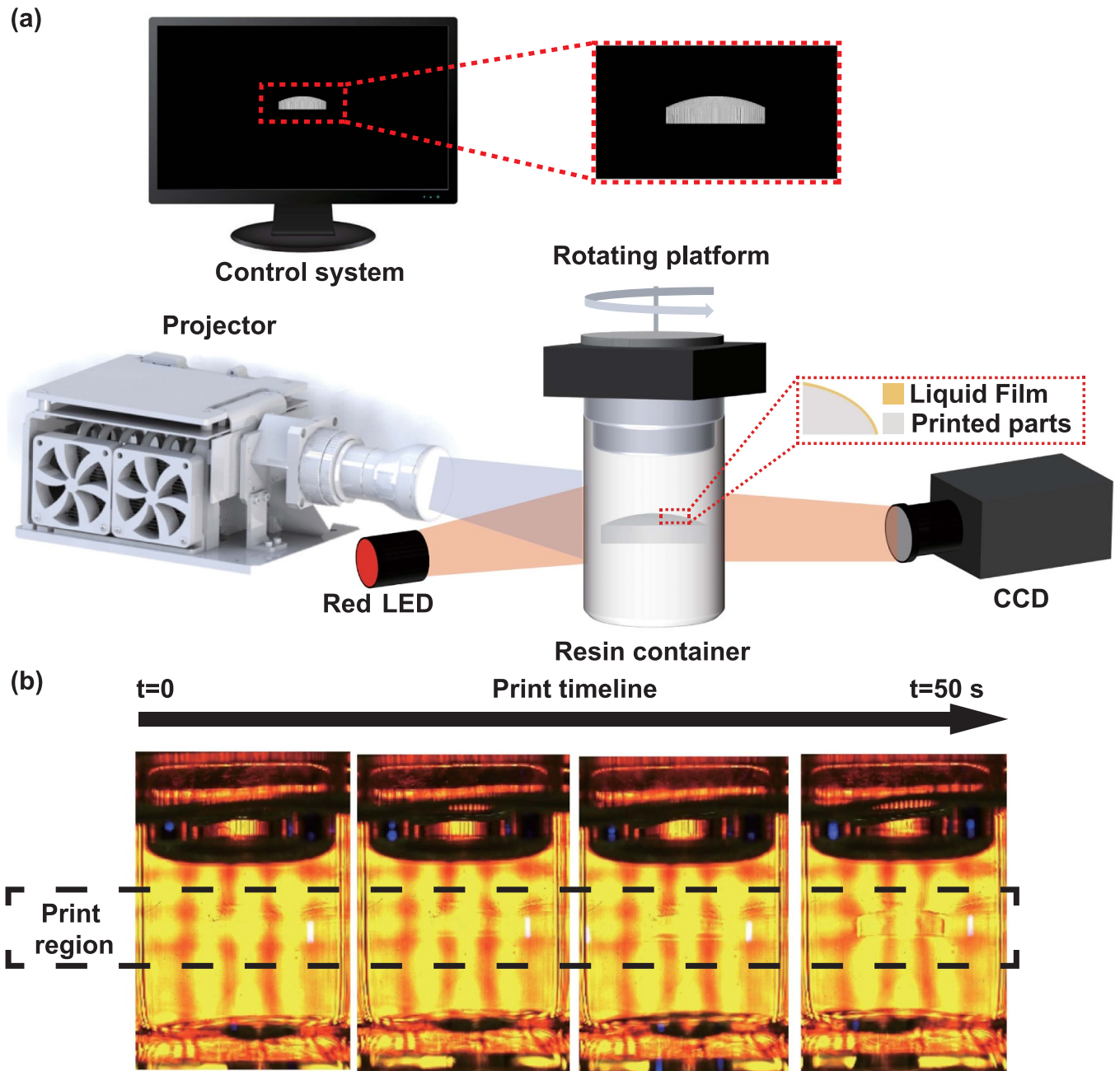
Figure 1. TVP system fabrication. (a) Schematic diagram of the critical components of the TVP system. (b) Sequential view of the TVP process. A centimeter-level convex lens is printed in less than a minute.

target region must absorb a minimum dose of light energy. After the accumulation of multi-angle projection doses, the target structure cures at once, as illustrated in figure 1(b) and movies S(1)–(2) of the supplementary materials.

2.2. Light dose calibration

In material systems for volumetric additive manufacturing, the concentration of the photoinitiator is a critical parameter. As an example, we used two acrylates polymerized via a free radical mechanism for printing. Specific material proportions can be seen in section 5. In the early period of printing, the activation of light leads to the production of free radicals that are rapidly suppressed and deactivated by oxygen, which is

necessary to produce a 3D dose in a given space. It is important to note that in TVP process, the entire build volume must be processed through each light pattern for the object to be reconstructed accurately. This function sets the upper limit of the photoinitiator concentration. From the spectrophotometer measurements shown in figure 2(a), the absorbance value of the 3:1 BPAGDA/PEGDA mixture is pretty low at the peak illumination wavelength of 405 nm, which is sufficient for binary printing in our system. Lower absorption is more conducive to light penetration in the resin without the photoinitiator.

A high-viscosity resin is required to counteract the printed object's sedimentation. In TVP, the increase in density of the liquid resin after solidification leads to its settling in the resin tank. It also benefits the resolution of the print since the
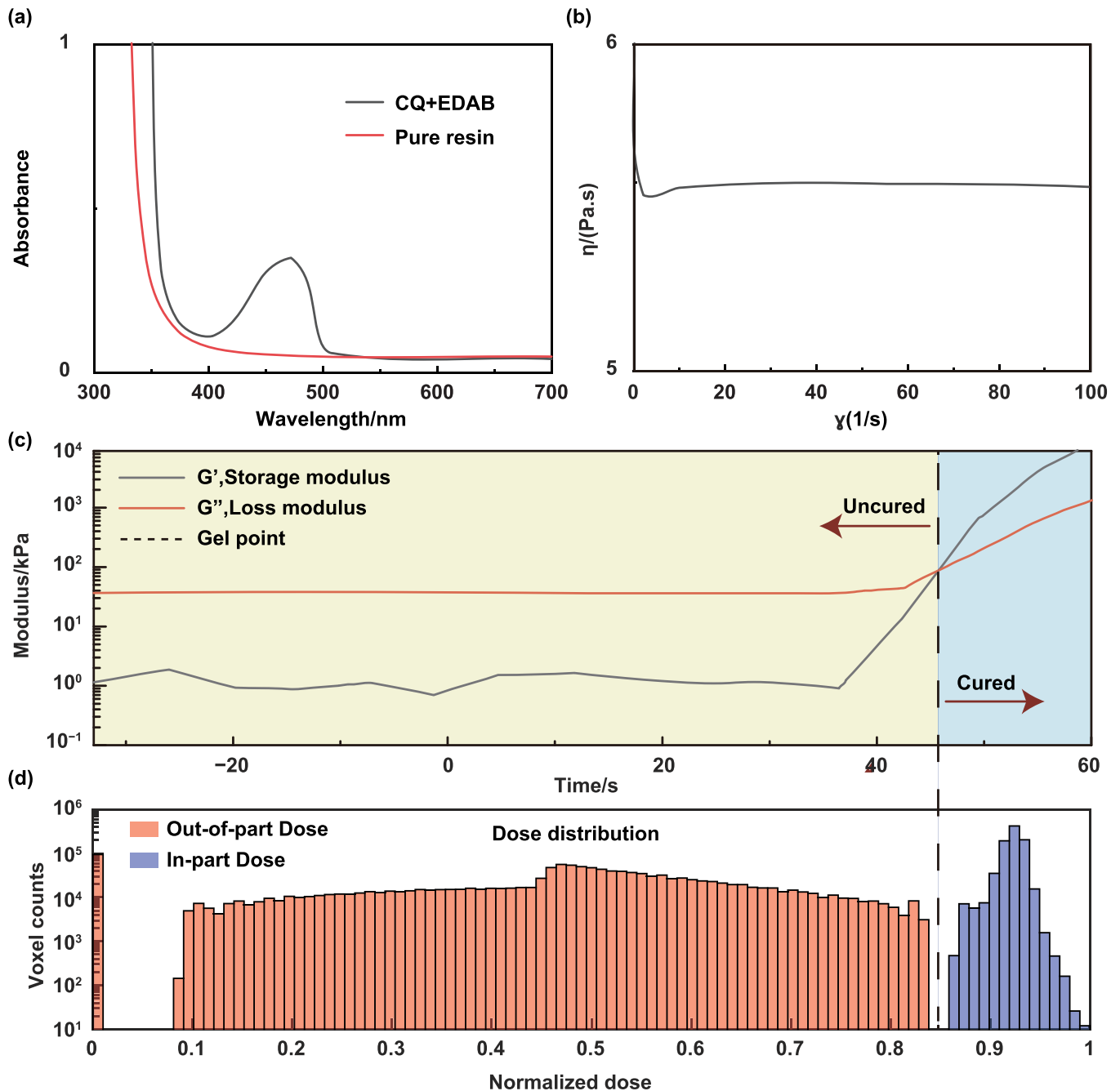
Figure 2. Adjustment of resin kinetics for TVP process. (a) The optical absorption spectrum of the lens material. (b) The rheological behavior of resins. (c) Binary printing process by real-time FTIR rheological analysis under 405 nm light. (d) In-part and out-of-part dose histogram of binary printing, in normalized units.

diffusion blur of the dose distribution is reduced. The viscosity of this polymer mixture was measured by a rheometer, as shown in figure 2(b). The viscosity is about 5.5 Pa·s in the range of shear strain rate 10 s^{-1} to 100 s^{-1}. Using the CCD camera observations, no significant precipitation (see figure S3 and movies S(1)–(2) of supplementary materials) could be measured within the manufacturing time, indicating a negligible effect on the print resolution in our current setup.

Figure 2(c) shows the adjustment of the induction period measured by using real-time Fourier transform infrared (FTIR) photorheology. The system solidifies when the storage

modulus exceeds the loss modulus (G′ > G″). The experiments were conducted at a light intensity of 7 mW cm^{-2}, and the gelation point corresponds to a time of approximately 45 s in our acrylic resin system. We further explored the effect of light intensity on the induction period. As shown in figure S4 of supplementary materials, with the increasing light intensity, the reaction gelation point time was accelerated along with a slight increase in the conversion rate of vinyl. As demonstrated in figure 2(d), the binary printing histogram primarily comprises two parts. 'In part' voxels (blue) inside the target space should exceed the dose corresponding to the gelation
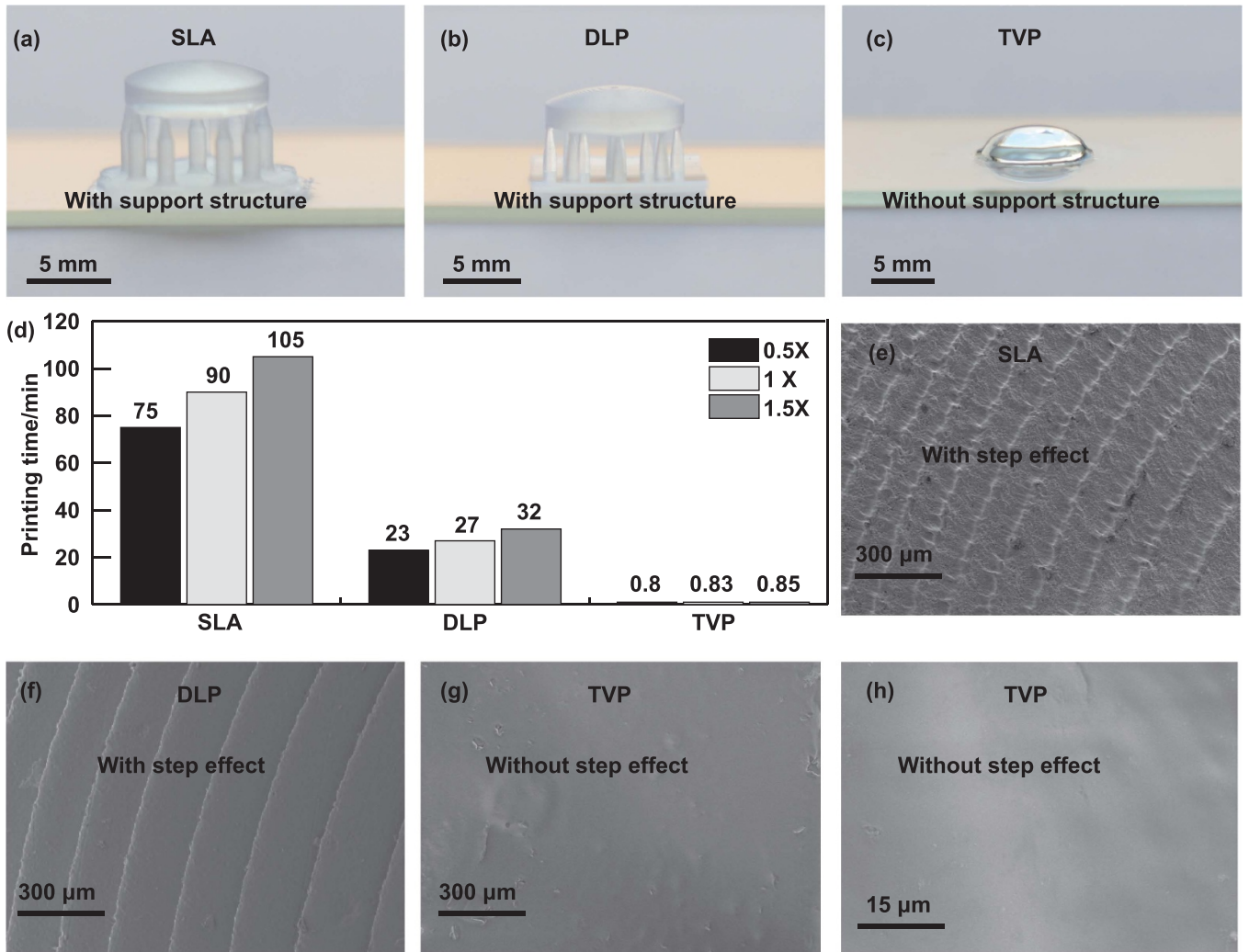
Figure 3. Surface topography characterization and printing time comparison of the printed the same lens by different light curing printing techniques. (a)–(c) The same model that SLA, DLP, and TVP fabricated. (d) Fabrication time for the lens model scaled 0.5 × (16.1 mm³), 1 × (128.6 mm³), and 1.5 × (434.1 mm³) using different light curing printing techniques. (e)–(g) SEM micrograph of the lens fabricated by SLA, DLP, and TVP before meniscus coating. (h) A close-up view of (g). Scale bars: (a)–(c) 5 mm, (e)–(g) 300 μm, and (h) 15 μm.

point. And 'Out of part' voxels (red), outside the target space, should remain in the liquid state. The projection sequence is optimized iteratively to maximize the separation between 'partial' and 'extra-partial' groups, which facilitates improved tolerance of imperfect optics and material [35].

3. Results and discussions

Binary printing satisfies the simultaneous curing of target points in space and has ultra-fast printing speed while ensuring a smooth surface. To verify that the TVP-printed samples have excellent surface quality, we printed the same model (Thorlabs, LA1472) using SLA, DLP, and TVP as shown in figures 3(a)–(c), under the same layer thickness (50 μm), respectively, with the printing parameters shown in table S1 of supplementary materials. TVP was performed in a high-viscosity resin. The lower fluidity ensures that the sample is in suspension, thus avoiding the challenges of a printing process that requires support, as illustrated in figures 3(a)–(c). That is

highly beneficial for printing optics, eliminating the limitation of damaging the surface of the optics during the removal of the support.

In addition, TVP has an absolute advantage in terms of printing speed. To quantify and compare printing times, we printed the above model, which has a volume of ≈ 128.6 mm³, then scaled down by 0.5× and up by 1.5× (volumes of ≈ 16.1 mm³ and 434.1 mm³, respectively). All TVP-printed models were completed within almost the same printing time (50 s), and in SLA, the print time increased rapidly with the scale factor. In contrast, in the DLP process, the print time grows linearly with increasing build height, regardless of the area to be printed in every layer (figure 3(d)). We compared the surface morphology using scanning electron microscopy (SEM) to characterize the same model printed with SLA, DLP, and TVP in figures 3(e)–(g). The apparent step effect can be found in figures 3(e) and (f), but not reflected in figures 3(g) and (h). The samples fabricated by TVP have excellent surface topography compared with the other two printing methods.
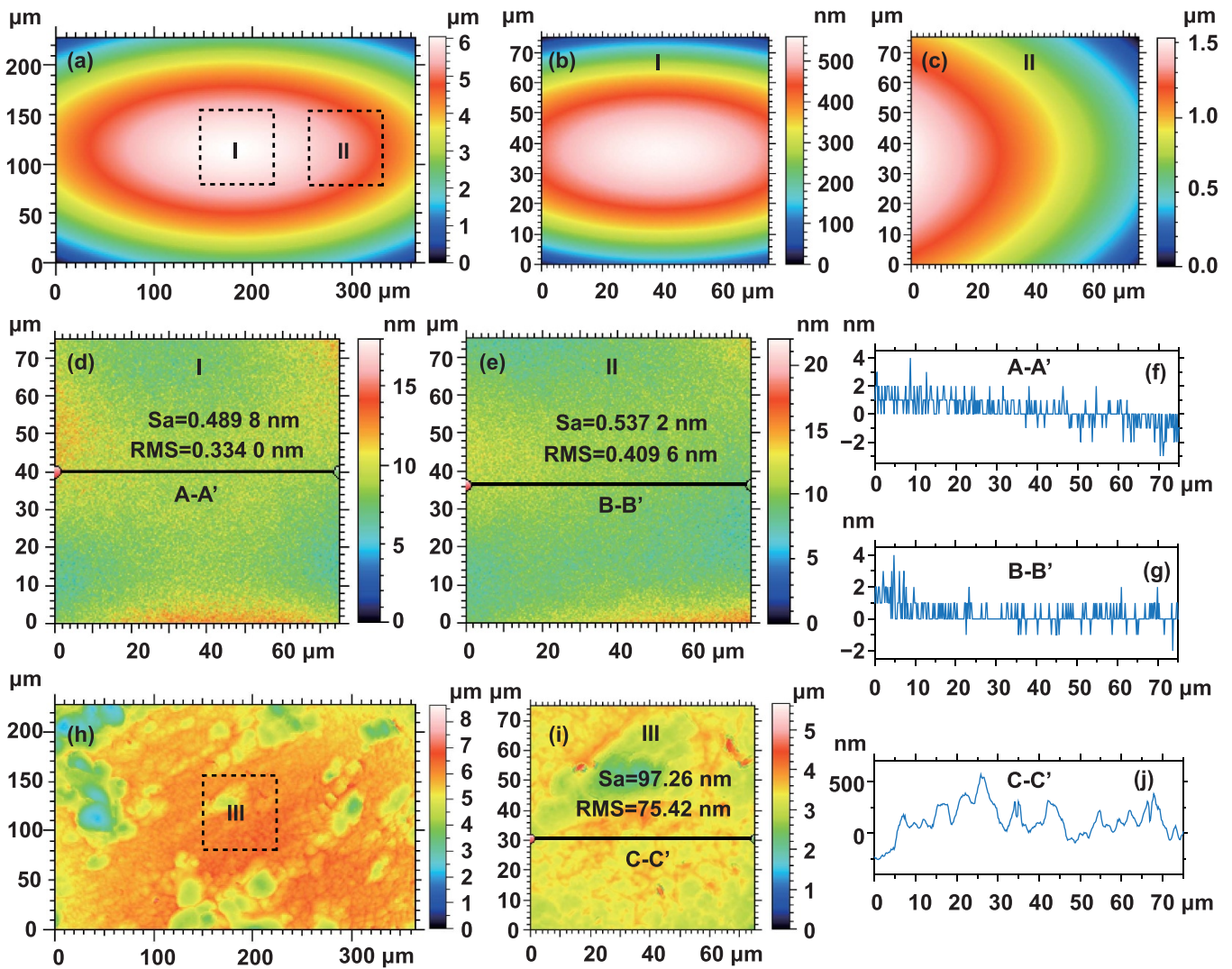
Figure 4. The 3D morphology of the TVP-printed lens. (a) The optical surface profiler captures the surface form of TVP-printed lens meniscus coating. (b) Magnified surface morphology of region I and (c) region II. (d) 3D roughness ingredients of the region I and (e) region II. (f) The cross-sectional A–A′ and (g) B–B′ profile of the roughness. (h) TVP fabricates the surface form of the lens without meniscus coating. (i) 3D roughness ingredients of region III.(j) The cross-sectional C–C′ profile.

However, we also noticed that the surface of the printed lens was damaged after cleaning, as shown in figure 3(g) and figure S5(b) of supplementary materials. As a demonstration, the lens fabricated with TVP after meniscus coating shows excellent light transmission performance and enables a clear view of the background image shown in figure S5(a).

The 3D morphology of the TVP-printed lens was quantitatively characterized by a white light interferometer with a pixel size of 0.19 nm. The results tested from the TVP-printed lens combined with the meniscus equilibrium post-curing method are shown in figures 4(a)–(g). Using the 50× objective lens of the white light interferometer, a randomly selected area over the vertex shown in figure 4(a) was used to compute the surface roughness. Figures 4(b) and (c) illustrate the enlarged forms of the two regions of the center (Region I) and the edge (Region II) extracted from figure 4(a). In figures 4(d) and (e), by statistical analysis, root mean square roughness (RMS) and the mean roughness (Sa) values at the center region I were found

to be 0.3340 nm and 0.4898 nm, respectively. The corresponding values in edge region II were 0.4096 nm and 0.5372 nm, which are considerably smaller compared to the wavelength of visible light, indicating that TVP process can produce optical devices with excellent surface quality when combined with the meniscus equilibrium post-curing method. In addition, the cross-sectional profiles in figures 4(f) and (g) extracted from figures 4(d) and (e) show a variation within ±4 nm without special features, which is very well suited for optical applications.

To demonstrate the significance of utilizing the meniscus equilibrium post-curing method to improve the surface finish of lenses manufactured through the TVP process, we removed the resin liquid film with isopropyl alcohol and characterized its surface quality. The cleaned surface is significantly rougher, as illustrated in figures 4(h)–(j). Figure 4(i) shows an arbitrary region selected from figure 4(h), resulting in statistical Sa = 97.26 nm and RMS = 75.42 nm, which did not
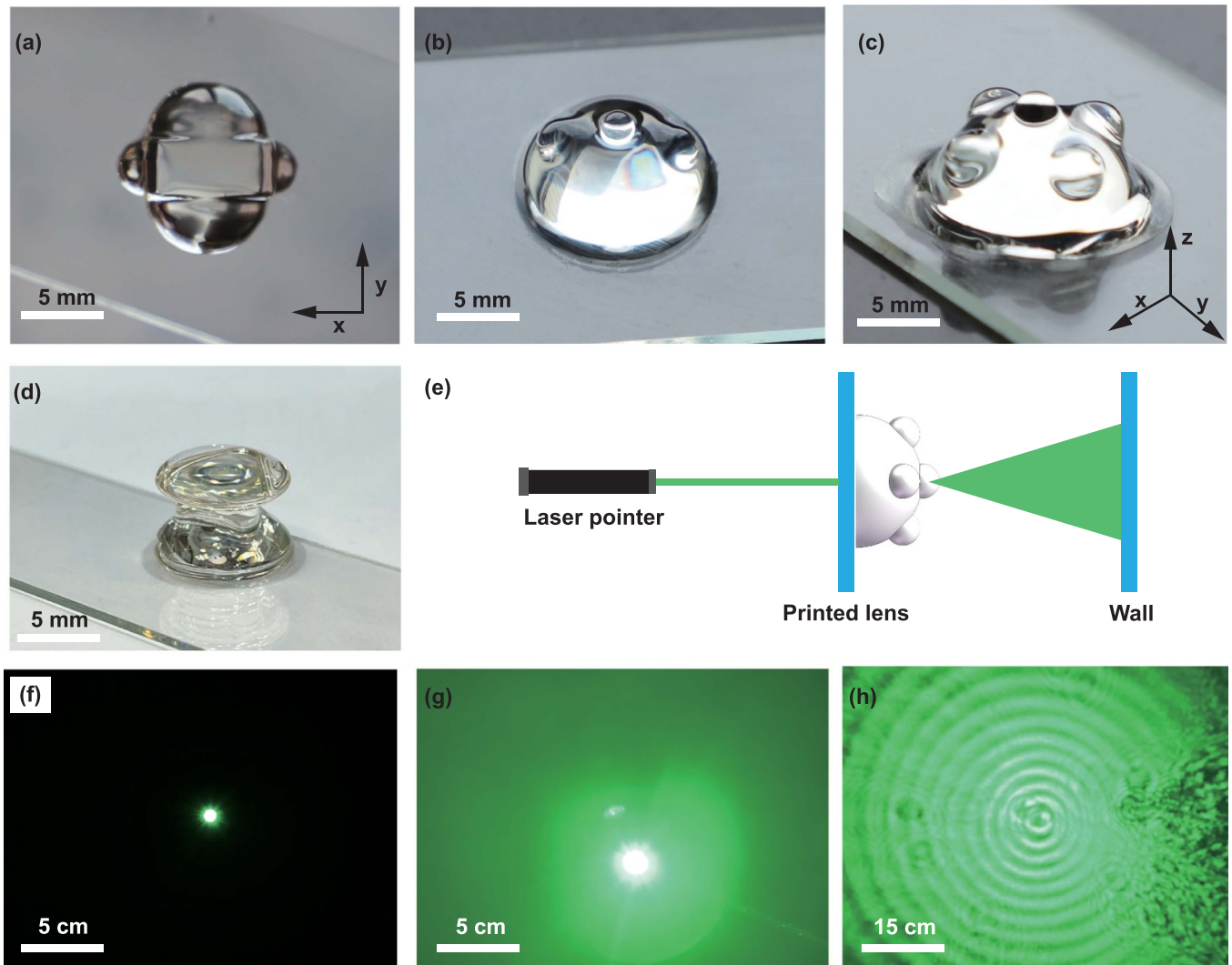
Figure 5. Fabrication of more complicated lenses (a)–(c) The images of complex shaped lenses. (d) The image of an assembly of two lenses. (e) The schematic diagram of the experimental optical system was used to demonstrate the functional properties of 3D-printed customized lenses. (f) Imaging of the green laser pointer without a complex lens. (g) Imaging of the green laser pointer across the *y*-axis in (a). (h) Imaging of the green laser pointer across the *z*-axis in (c). scale bars: (a)–(d) 5 mm, (f)–(g) 5 cm, and (h) 15 cm.

satisfy the strict $\lambda/20$ criterion. To verify the print versatility of the meniscus equilibrium post-curing method combined with TVP in optical devices, the same sphere lens was also printed using another resin (see the details in section 5). As shown in figure S6 of supplementary materials, the values of two roughness parameters, RMS and Sa, were obtained through statistical analysis as RMS = 0.3340 nm and Sa = 0.5199 nm, suggesting the meniscus equilibrium effect well-smoothed surface topography. It was noticed that the the resin film remaining on TVP- printed lens did not fully post-cure. After extracting the target structure from the resin, the photoinitiator is almost consumed in the resin film, making it difficult to perform a fully post-cured treatment.

In conclusion, the results obtained were listed in table S2 of supplementary materials and three other cases of 3D printing using projection stereolithography printing. Energy modulation using the volumetric method has a definite advantage in printing speed. However, the single-angle volumetric energy modulation [21] necessitates a support structure to house the printed lens. In our work, multi-angle projection (figure S7) in a high-viscosity resin for light dose delivery can generate the target body simultaneously after reaching the energy threshold, as shown in figure S8. Furthermore, the layerwise approach and TVP process make it easier to control the printing shape. However, the layer-based printing method inevitably has a step effect, which requires additional complex processes to eliminate the step effect (supplementary table S3). Since TVP prints all the basic points of the entity at the same time, there is no step effect as shown in figures 3(g) and (h).

Other complicated lenses (figures 5(a)–(c)) and a lens set (figure 5(d)) were also printed using the TVP process. As shown in figure 5(e), we used a simple setup to test the functional properties of the TVP-printed lens. As illustrated in figure 5(f), without a 3D printing lens, the light from the green laser pointer displayed a dot on the wall. Figure 5(g) shows the results after the laser passes through the *y*-direction in figure 5(a). The spot diameter changes significantly after the beam passes through the biconvex lens. More interestingly, as
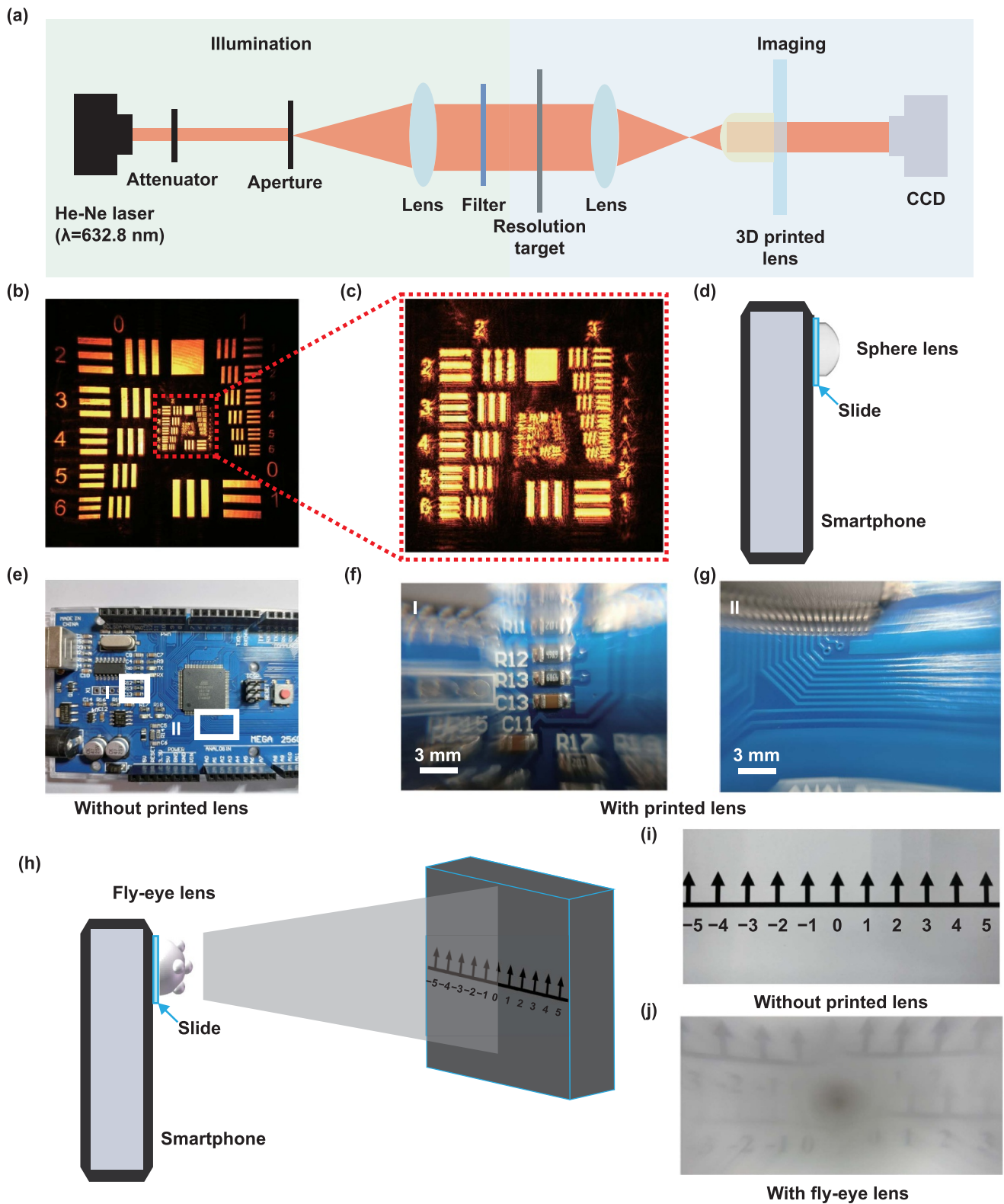
Figure 6. Imaging characteristics of TVP-printed lenses. (a) Schematic diagram of the experimental system for characterizing the imaging performance of the TVP-printed custom lens. (b) Image of the embedded printed lens capturing the resolution test target. (c) Close-up view of group 2 and 3 components. (d) The schematic of the setup using the sphere lens. (e) The image of a circuit board captured by a smartphone without using the spherical lens. (f) and (g) Two magnified images captured from (e) using the spherical lens. (h) The schematic of the setup using the fly-eye lens. (i) The image of a plate with engraved coordinates captured by a smartphone without using the printed lens and (j) using the fly-eye lens.

the beam passes along the *Z*-direction in figure 5(c), the wall shows enlarged light and dark streaks, indicating the fly-eye lens with a wide-angle field of view (figure 5(h)). This suggests that the optics fabricated by TVP combined with the meniscus equilibrium post-curing method can be more functional with a different design. To investigate the dimensional accuracy acquired by the TVP, we have designed several standard structures to compare the geometric measurements of the printed parts with the CAD models, as illustrated in figure S9(a). Figure S9(b) shows the geometric dimensions of the printed samples (3:1 BPAGDA/PEGDA) deviate from the design values by about 2.2% to 8.0%.

Upon successfully validating the improved surface quality of the TVP-printed lens in combination with the meniscus equilibrium post-curing method, we further explored TVP's ability to customize imaging lenses, using a spherical lens as a representative example. As shown in figure S10, the cured part shows an excellent transmittance of nearly 90% in the visible range measured by a UV–vis spectrophotometer. Figure S11 illustrates the refractive index values (*N*) of the photopolymerized acrylate resin at different wavelengths, which were measured using a spectroscopic ellipsometer. The geometry and optical properties of a typical spherical lens were designed and optimized in Zemax using a complex refractive index as input. The insert in figure S11 of supplementary materials illustrates optical simulation of the imaging properties for the optimized design of the spherical lens.

To demonstrate the optical property of the TVP-printed lens, an experimental setup in figure 6(a) used a resolution test target (GCG-020601, Daheng New Epoch Technology, Inc.) which has eight groups of patterns from 0 to +7. Figure 6(b) shows the target image captured by the CCD. Figure 6(c) shows that the bars in element 6 of group 3 can be seen. The TVP-printed spherical lens was attached to a smartphone, shown in figure 6(d), for a quick demonstration. Figure 6(e) shows an image of the surface of the Arduino Mega 2560 taken through a smartphone without using the printed lens. Two magnified images of the surface of the Arduino Mega 2560 were captured through the smartphone by using a spherical lens, as shown in figures 6(f) and (g). We can visualize the component type in focus and the line with a width of 500 μm. Here, we employed a coordinate line as an object shown in figure 6(i). The fabricated fly-eye lens was directly mounted onto a smartphone shown in figure 6(h), and we found that magnified object image was observed in figure 6(j). The imaging magnification was due to the function of a convex lens for magnified imaging, and the formation of two blurred coordinate lines showed that we could get the image from the ommatidium, which had been reported in the earlier studies [36, 37]. The testing results confirmed that the TVP-printed lens could be effectively utilized in commercial smartphones to deliver high-quality images.

4. Conclusion

In this work, we have combined the meniscus equilibration post-curing method with the TVP process to reduce surface roughness of manufactured object to the nanometer level while maintaining high manufacturing speeds. The entire object was polymerized in a single step under the irradiation of a series of modulated UV light patterns. As a demonstration, centimeter-scale spherical and complex lenses were printed directly in less than one minute. The spherical lens was printed at the speed of 3.1×10^4 mm^3 h^{-1} with an average roughness of RMS = 0.3340 nm. The printed components deviate from the design values by 2.2% to 8.0%. Mounting the TVP-printed lens directly onto the smartphone's rear camera and capturing a sharp picture of the Arduino Mega 2560 demonstrates the practicality of using TVP-printed lenses for optical imaging. The current design of the TVP printing technique is only feasible for high-viscosity materials, which can be dragged to rotate at almost the same speed as the motor. This limits the promotion of the printing speed threshold. Furthermore, applying a meniscus liquid film adhering to the printed surface is relied on oxygen-induced polymerization inhibition and causes incomplete curing of the printed 3D part. Process improvements should be further studied for higher speed, multi-material applications. In summary, the work presented in this paper shows the potential of TVP technology for applications in the optical field. It is predicted that TVP will become a powerful technology in fabricating complex optical devices.

5. Experimental section

5.1. Preparation of photocurable resin

The photocurable resin is prepared by mixing bisphenol A glycerolate (1 glycerol/phenol) diacrylate (refractive index = 1.557) and poly(ethylene glycol) diacrylate (refractive index = 1.463, average Mn = 250) at a mass ratio of 3:1. Camphorquinone (CQ) was used as the photoinitiator with a mass fraction of one-thousandth of the above-mixed resin. Ethyl 4-dimethylaminobenzoate (EDAB) of comparable mass to CQ was used as a co-initiator. These chemicals were purchased from Sigma-Aldrich (Shanghai) Trading Co., Ltd and can be used directly without further purification. In addition, an alternative alphatic urethane acrylate resin (WDS-3532) purchased from Wuxi Boqiang Polymer materials science and technology CO., Ltd with a viscosity range of 1.2–3.6 Pa·s was used to fabricate the sphere lens. To limit the attenuation of the optical path in the resin, the mass of CQ and EDAB is one-thousandth of the total mass, respectively.

5.2. Volumetric additive manufacturing system

Figure 1(a) shows the hardware system design in this study. The process of TVP of complex-shaped lens was carried out using a DLP projector ((PRO4500, Wintech, China) with an optical lens (*f* = 150 mm). The UV projector was capable of providing a maximal projection area of 96 mm × 54 mm and a light intensity range of 0–34.7 mW cm^{-2}. The printing process (movies S(1)–(2) of supplementary materials) is captured via a CCD camera (MER2-503-36U3C, Daheng New Epoch Technology, Inc.) in the arrangement shown in figure 1. A 21 mm diameter cylindrical vial containing photosensitive resin was mounted to a motorized rotation stage (URS50BCC,

Newport) with a custom-designed vial holder. A large rectangular vat containing the index-matching solution is outside the cylindrical vial. The wall of the vat is perpendicular to the incident beam.

5.3. TVP post-treatment

After printing, to reduce the viscosity of uncured material, the vials containing the uncured material and cured part were heated in a water bath at 60 °C for 10–20 s. After extracting the manufactured object from the resin container, the resin film remaining on its surface because of the wetting and capillary phenomena. The prints were subjected to post-curing using 405 nm light within a Formlabs Form Cure machine at a temperature of 60 °C for 20 min.

5.4. Characterization

The viscosity of the mixed acrylic resin solutions were characterized by a rheometer (HAAKE MARS, America) at room temperature. The absorption spectrum of the monomer and the transmission spectrum of the cured parts were recorded using a UV–vis spectrophotometer (UV1800, Shimadzu, Japan). As shown in figure S4, real-time FTIR rheological analysis was carried out under 405 nm light irradiation using a device combining rheometer (HAAKE MARS60, ThermoFisher) and ATR-FTIR (Nicolet iS10 series, ThermoFisher). A spectroscopic ellipsometer (ME-L, Wuhan Eoptics Technology Co., Ltd, China) measured the wavelength-dependent refractive index. The surface morphology of three 3D printed lenses was investigated using SEM (Sigma 300, ZEISS, Germany). An optical surface profiler based on white light interferometry (ER230, Atometrics, China) was utilized to catch the 3D morphology of the TVP-printed lens. Measurements were made with a 50x objective lens (Nikon 50x Mirau) to obtain the surface morphology.

Acknowledgments

ORCID iD

Yu Liu https://orcid.org/0000-0002-7945-7462

References

[1] Zhu Y Z *et al* 2022 Recent advancements and applications in 3D printing of functional optics *Addit. Manuf.* **52** 102682
[2] Oulton R F, Flórez J and Clark A S 2022 Ferroelectric nanosheets boost nonlinearity *Nat. Photon.* **16** 611–2
[3] Choi W, Kang M, Hong J H, Katz O, Lee B, Kim G H, Choi Y and Choi W 2022 Flexible-type ultrathin holographic endoscope for microscopic imaging of unstained biological tissues *Nat. Commun.* **13** 4469
[4] Zhao L, Wu B, Niu Y, Zhu S K, Chen Y, Chen H Y and Chen J-H 2022 Soft optoelectronic sensors with deep learning for gesture recognition *Adv. Mater. Technol.* **7** 2101698
[5] Reddy J W, Kimukin I, Stewart L T, Ahmed Z, Barth A L, Towe E and Chamanzar M 2019 High density, double-sided, flexible optoelectronic neural probes with embedded μLEDs *Front. Neurosci.* **13** 745
[6] Meng S T, Yin Z Q, Guo Y W, Yao J H and Chai N 2020 Ultra-precision machining of polygonal Fresnel lens on roller mold *Int. J. Adv. Manuf. Technol.* **108** 2445–52
[7] Peixoto C, Valentim P T, Sousa P C, Dias D, Araújo C, Pereira D, Machado C F, Pontes A J, Santos H and Cruz S 2022 Injection molding of high-precision optical lenses: a review *Precis. Eng.* **76** 29–51
[8] Zolfaghari A, Chen T T and Yi A Y 2019 Additive manufacturing of precision optics at micro and nanoscale *Int. J. Extrem. Manuf.* **1** 012005
[9] Ge Q, Li Z Q, Wang Z L, Kowsari K, Zhang W, He X N, Zhou J L and Fang N X 2020 Projection micro stereolithography based 3D printing and its applications *Int. J. Extrem. Manuf.* **2** 022004
[10] Yuan C, Kowsari K, Panjwani S, Chen Z C, Wang D, Zhang B, Ng C J X, Alvarado P V Y and Ge Q 2019 Ultrafast three-dimensional printing of optically smooth microlens arrays by oscillation-assisted digital light processing *ACS Appl. Mater. Interfaces* **11** 40662–8
[11] Zhang Y, Wu L, Zou M M, Zhang L D and Song Y L 2022 Suppressing the step effect of 3D printing for constructing contact lenses *Adv. Mater.* **34** 2107249
[12] Chen X F, Liu W Z, Dong B Q, Lee J, Ware H O T, Zhang H F and Sun C 2018 High-speed 3D printing of millimeter-size customized aspheric imaging lenses with sub 7 nm surface roughness *Adv. Mater.* **30** 1705683
[13] Chen L, Duan G H, Zhang C, Cheng P and Wang Z L 2022 3D printed hydrogel for soft thermo-responsive smart window *Int. J. Extrem. Manuf.* **4** 025302
[14] Nair P S, Trisno J, Wang H T and Yang J K W 2021 3D printed fiber sockets for plug and play micro-optics *Int. J. Extrem. Manuf.* **3** 015301
[15] Kotz F, Quick A S, Risch P, Martin T, Hoose T, Thiel M, Helmer D and Rapp B E 2021 Two-photon polymerization of nanocomposites for the fabrication of transparent fused silica glass microstructures *Adv. Mater.* **33** 2006341
[16] Wang Y, Gawedzinski J, Pawlowski M E and Tkaczyk T S 2018 3D printed fiber optic faceplates by custom controlled fused deposition modeling *Opt. Express* **26** 15362–76
[17] Kong Y L, Tamargo I A, Kim H, Johnson B N, Gupta M K, Koh T-W, Chin H-A, Steingart D A, Rand B P and Mcalpine M C 2014 3D printed quantum dot light-emitting diodes *Nano Lett.* **14** 7017–23
[18] Jeong H Y, Lee E, An S-C, Lim Y and Jun Y C 2020 3D and 4D printing for optics and metaphotonics *Nanophotonics* **9** 1139–60
[19] Shao G B, Hai R H and Sun C 2020 3D printing customized optical lens in minutes *Adv. Opt. Mater.* **8** 1901646
[20] Vaidya N and Solgaard O 2018 3D printed optics with nanometer scale surface roughness *Microsyst. Nanoeng.* **4** 18
[21] Xu Y, Huang P, To S, Zhu L-M and Zhu Z W 2022 Low-cost volumetric 3D printing of high-precision miniature lenses in seconds *Adv. Opt. Mater.* **10** 2200488
[22] Alam F, Elsherif M, AlQattan B, Salih A, Lee S M, Yetisen A K, Park S and Butt H 2021 3D printed contact lenses *ACS Biomater. Sci. Eng.* **7** 794–803

[23] Pan Y Y and Chen Y 2016 Meniscus process optimization for smooth surface fabrication in stereolithography *Addit. Manuf.* **12** 321–33

[24] Pan Y Y and Chen Y 2015 Smooth surface fabrication based on controlled meniscus and cure depth in microstereolithography *J. Micro Nano-Manuf.* **3** 031001

[25] Shusteff M, Browar A E M, Kelly B E, Henriksson J, Weisgraber T H, Panas R M, Fang N X and Spadaccini C M 2017 One-step volumetric additive manufacturing of complex polymer structures *Sci. Adv.* **3** eaao5496

[26] Rodríguez-Pombo L, Xu X Y, Seijo-Rabina A, Ong J J, Alvarez-Lorenzo C, Rial C, Nieto D, Gaisford S, Basit A W and Goyanes A 2022 Volumetric 3D printing for rapid production of medicines *Addit. Manuf.* **52** 102673

[27] Regehly M, Garmshausen Y, Reuter M, König N F, Israel E, Kelly D P, Chou C-Y, Koch K, Asfari B and Hecht S 2020 Xolography for linear volumetric 3D printing *Nature* **588** 620–4

[28] Kelly B E, Bhattacharya I, Heidari H, Shusteff M, Spadaccini C M and Taylor H K 2019 Volumetric additive manufacturing via tomographic reconstruction *Science* **363** 1075–9

[29] Toombs J T, Luitz M, Cook C C, Jenne S, Li C C, Rapp B E, Kotz-Helmer F and Taylor H K 2022 Volumetric additive manufacturing of silica glass with microscale computed axial lithography *Science* **376** 308–12

[30] Bernal P N, Delrot P, Loterie D, Li Y, Malda J, Moser C and Levato R 2019 Volumetric bioprinting of complex living-tissue constructs within seconds *Adv. Mater.* **31** 1904209

[31] Loterie D, Delrot P and Moser C 2020 High-resolution tomographic volumetric additive manufacturing *Nat. Commun.* **11** 852

[32] Cook C C *et al* 2020 Highly tunable thiol-ene photoresins for volumetric additive manufacturing *Adv. Mater.* **32** 2003376

[33] Wang B, Engay E, Stubbe P R, Moghaddam S Z, Thormann E, Almdal K, Islam A and Yang Y 2022 Stiffness control in dual color tomographic volumetric 3D printing *Nat. Commun.* **13** 367

[34] Madrid-Wolff J, Boniface A, Loterie D, Delrot P and Moser C 2022 Controlling light in scattering materials for volumetric additive manufacturing *Adv. Sci.* **9** 2105144

[35] Rackson C M, Champley K M, Toombs J T, Fong E J, Bansal V, Taylor H K, Shusteff M and Mcleod R R 2021 Object-space optimization of tomographic reconstructions for additive manufacturing *Addit. Manuf.* **48** 102367

[36] Hu Z-Y, Zhang Y-L, Pan C, Dou J-Y, Li Z-Z, Tian Z-N, Mao J-W, Chen Q-D and Sun H-B 2022 Miniature optoelectronic compound eye camera *Nat. Commun.* **13** 5634

[37] Li M J, Yang T Z, Yang Q, Fang Z, Bian H, Zhang C J, Hou X and Chen F 2022 Bioinspired anti-fogging and anti-fouling artificial compound eyes *Adv. Opt. Mater.* **10** 2200861